nature COMMUNICATIONS

ARTICLE

DOI: 10.1038/s41467-017-00427-5 OPEN

High-quality monolayer superconductor $NbSe_2$ grown by chemical vapour deposition

Hong Wang[1,2], Xiangwei Huang[3], Junhao Lin[4], Jian Cui[3,5], Yu Chen[6], Chao Zhu[1], Fucai Liu[1], Qingsheng Zeng[1], Jiadong Zhou[1], Peng Yu[1], Xuewen Wang[1], Haiyong He[1], Siu Hon Tsang[7], Weibo Gao[6], Kazu Suenaga[4], Fengcai Ma[5], Changli Yang[3,8], Li Lu[3,8], Ting Yu[6], Edwin Hang Tong Teo[2,7], Guangtong Liu[3] & Zheng Liu[1,2,9]

The discovery of monolayer superconductors bears consequences for both fundamental physics and device applications. Currently, the growth of superconducting monolayers can only occur under ultrahigh vacuum and on specific lattice-matched or dangling bond-free substrates, to minimize environment- and substrate-induced disorders/defects. Such severe growth requirements limit the exploration of novel two-dimensional superconductivity and related nanodevices. Here we demonstrate the experimental realization of superconductivity in a chemical vapour deposition grown monolayer material—$NbSe_2$. Atomic-resolution scanning transmission electron microscope imaging reveals the atomic structure of the intrinsic point defects and grain boundaries in monolayer $NbSe_2$, and confirms the low defect concentration in our high-quality film, which is the key to two-dimensional superconductivity. By using monolayer chemical vapour deposited graphene as a protective capping layer, thickness-dependent superconducting properties are observed in as-grown $NbSe_2$ with a transition temperature increasing from 1.0 K in monolayer to 4.56 K in 10-layer.

[1] Centre for Programmable Materials, School of Materials Science and Engineering, Nanyang Technological University, Singapore 639798, Singapore. [2] NOVITAS, Nanoelectronics Centre of Excellence, School of Electrical and Electronic Engineering, Nanyang Technological University, Singapore 639798, Singapore. [3] Beijing National Laboratory for Condensed Matter Physics, Institute of Physics, Chinese Academy of Sciences, Beijing 100190, China. [4] National Institute of Advanced Industrial Science and Technology (AIST), Tsukuba 305-8565, Japan. [5] Department of Physics, Liaoning University, Shenyang 110036, China. [6] Division of Physics and Applied Physics, School of Physical and Mathematical Sciences, Nanyang Technological University, Singapore 637371, Singapore. [7] Temasek Laboratories@NTU, Nanyang Technological University, Singapore 639798, Singapore. [8] Collaborative Innovation Center of Quantum Matter, Beijing 100871, China. [9] Centre for Disruptive Photonic Technologies, School of Physical and Mathematical Sciences, Nanyang Technological University, Singapore 637371, Singapore. Hong Wang, Xiangwei Huang and Junhao Lin contributed equally to this work. Correspondence and requests for materials should be addressed to E.H.T.T. (email: htteo@ntu.edu.sg) or to G.L. (email: gtliu@iphy.ac.cn) or to Z.L. (email: z.liu@ntu.edu.sg)

Monolayer superconductors provide ideal models for investigating superconductivity in the two-dimensional (2D) limit, as well as superconductor-substrate interplay[1–5]. Strong enhancement of the transition temperature (T_c) has been reported in the monolayer FeSe/$SrTiO_3$ system[6, 7], which indicates that 2D ultra-thin films have the potential to be high-T_c superconductors. However, the superconductivity in most monolayers (Pb[8, 9], In[8, 10], FeSe[6]) only survives on certain substrates, probably due to particular interface bonds[6, 8]. Monolayer $NbSe_2$, has recently been recognized as an intrinsic monolayer superconductor, due to the occurrence of superconductivity without the need of a special substrate[4]. $NbSe_2$ crystallizes in the same layered hexagonal structure as 2*H*-MoS_2, where the niobium atoms sit at the center of trigonal selenium prisms. Compared with the bulk, 2D $NbSe_2$ exhibits significantly different properties arising from reduced dimensionality, as exemplified by the observation of Ising superconductivity[11], quantum metallic state[12], and strong enhancement of charge density wave order[4].

Defects in an ultrathin superconductor are known to be a critically detrimental factor to intrinsic 2D superconductivity[13, 14]. Monolayer ambient-sensitive[15, 16] $NbSe_2$ is predisposed to receive defects from the substrate and ambient environment. Therefore, the growth of superconducting $NbSe_2$ monolayers is a great challenge. Though superconducting $NbSe_2$ layers can be mechanically exfoliated from bulk $NbSe_2$ crystals, it is not a scalable method. Also, the thickness and size of exfoliated $NbSe_2$ flakes cannot be controlled. In the past few years, chemical vapour deposition (CVD) has been widely employed to synthesize ultrathin semiconducting transition metal dichalcogenides (TMDs) such as MoS_2 and WSe_2[17–24]. Recently, $NbSe_2$ multilayers were prepared by selenizing pre-deposited Nb_2O_5 films. However, none of the prepared $NbSe_2$ was found to be superconducting[25, 26], probably due to the large concentration of defects created during growth. Currently,

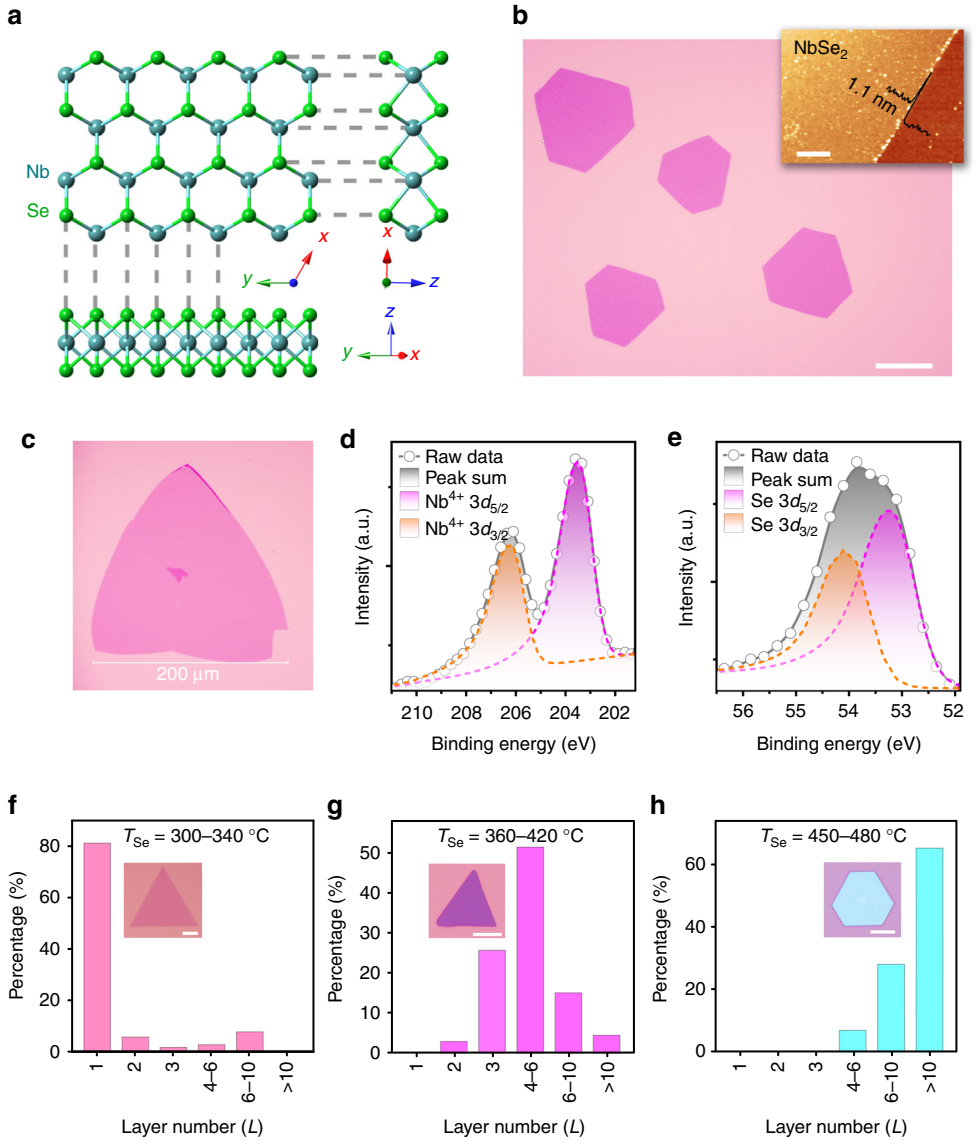

Fig. 1 Atomic structure, morphologies, and characterizations of $NbSe_2$ crystals. **a** Ball-and-stick model of monolayer 2*H*-$NbSe_2$ viewed from three different directions. **b** Optical image of uniform $NbSe_2$ crystals deposited on a SiO_2/Si substrate. *Scale bar*, 40 μm. A representative AFM image (*inset*; *scale bar*, 1 μm) shows the typical thickness is 1.1 nm. **c** A monolayer $NbSe_2$ crystal with edge length of 0.2 mm. **d**, **e** X-ray photoemission spectroscopy (*XPS*) spectra of the **d** Nb 3*d* and **e** Se 3*d* peaks from $NbSe_2$ crystals deposited on SiO_2/Si substrate. **f**–**h** Statistic thickness distributions and representative morphologies (*inset*) of $NbSe_2$ crystals synthesized with T_{Se} setting at **f** 300-340, **g** 360-420 and **h** 450-480 °C, respectively. *Scale bars* from *inset* of **f**–**h** are 20, 5 and 5 μm. Thickness of *inset* crystals of **f**–**h** are 1.1, 5.1 and 16.2 nm

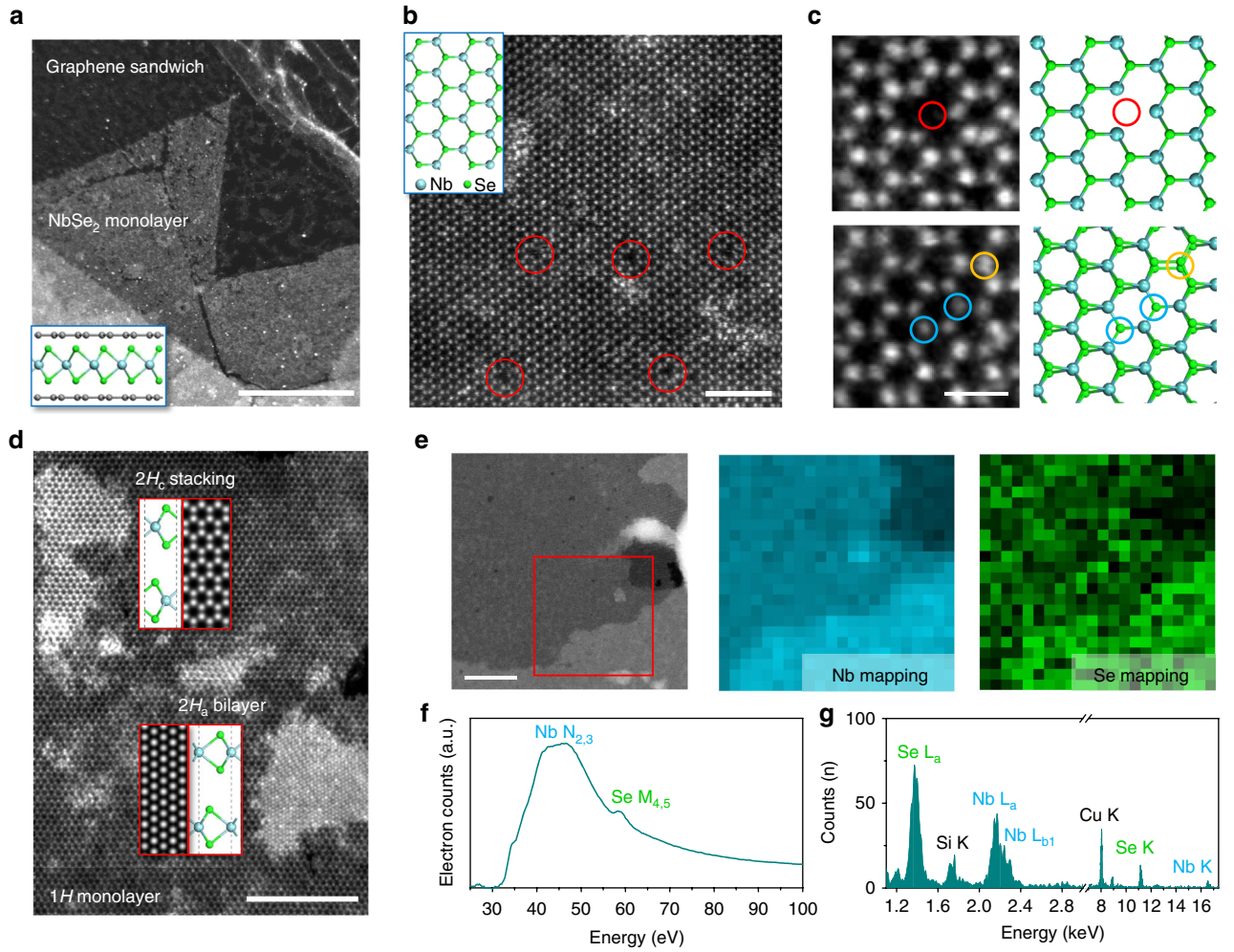

Fig. 2 ADF-STEM images, EELS, and EDX characterizations of the as-synthesized $NbSe_2$ atomic layers. **a** A low magnified annular dark-field scanning transmission electron microscope (*ADF-STEM*) image showing a large region of monolayer $NbSe_2$ encapsulated by the graphene sandwich. The schematic is shown in the *inset*. **b** Atomic resolution ADF-STEM image of the hexagonal $NbSe_2$ lattice. Diselenium vacancies are highlighted by *red circles*. The *inset* of panel **b** shows the structural model of 2*H*-$NbSe_2$, with *cyan* and *green color* indicating Nb and Se atoms, respectively. **c** Different point defects in monolayer $NbSe_2$ and their atomic models. Diselenium vacancy, monoselenium vacancy, and anti-site defect Se_{Nb} are highlighted by *red*, *blue*, and *yellow circles*, respectively. **d** Atomic resolution ADF-STEM image of two bilayer islands in $NbSe_2$, showing the coexistence of $2H_a$ and $2H_c$ stacking sequence. The *insets* are corresponding atomic models and simulated STEM images. **e** STEM image of a large region of $NbSe_2$ used for the collection of electron energy-loss spectroscopy (*EELS*) and energy-dispersive X-ray spectrometry (*EDX*) spectra. The collected region is highlighted in *red square*. Nb and Se EELS mapping are provided next to it. **f** Typical EELS and **g** EDX spectra of the region shown in **e**. The Cu signal in the EDX spectra comes from the Cu grid. *Scale bars*, 500 nm (**a**), 2 nm (**b**), 0.5 nm (**c**), 5 nm (**d**), 50 nm (**e**)

superconducting $NbSe_2$ monolayers can only be grown by molecular beam epitaxial (MBE) under ultrahigh vacuum (UHV) and on a dangling bond-free graphene or *h*-BN substrate[3, 27], in order to minimize environment- and substrate-induced disorders/defects. However, MBE is expensive to perform because it requires a high-priced apparatus and a UHV environment. Furthermore, MBE growth of $NbSe_2$ is only available on specific graphene and *h*-BN substrates[3, 27], and the individual domain size is $< 1\,\mu m$[3, 27]. Therefore, it is desirable to develop a facile growth method to produce high-quality superconducting $NbSe_2$ layers.

In this work, we report the growth of the monolayer superconductor $NbSe_2$ at ambient pressure on a variety of substrates. Atomic-resolution annual dark-field scanning transmission electron microscope (ADF-STEM) imaging reveals the atomic structure of the intrinsic defects in the as-grown monolayer $NbSe_2$ crystal, such as point defects and grain boundaries, and confirms the low concentration of defects in both mono- and few-layer regions. Transport data indicate that even low concentration of defects exist in CVD-grown $NbSe_2$, they will not significantly affect the superconducting properties.

Results

Growth of monolayer $NbSe_2$ crystals. Atomically thin $NbSe_2$ crystals were grown on diverse substrates by ambient pressure CVD in a tube furnace (Supplementary Fig. 1). Partially oxidized niobium powder NbO_x ($x \leq 2.5$) was chosen as the precursor (Supplementary Fig. 2). Briefly, the powder mixture of NbO_x and NaCl was loaded in an alumina boat into the center of a fused quartz tube. Diverse substrates (SiO_2/Si, Si(100), quartz, etc.) were placed 1-3 mm above the powder mixture with the polished side faced down. Selenium powder was located at the entrance of the tube furnace, where the temperature was 300–340 °C during growth. Further details of the experiments are provided in the "Methods" section. Figure 1a shows the crystal structure of

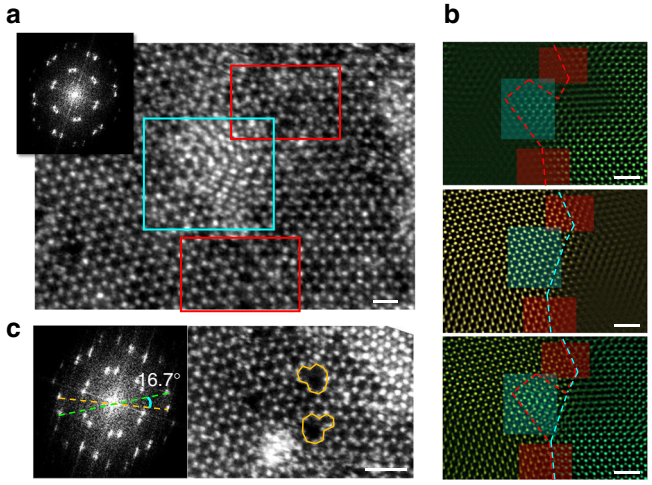

Fig. 3 ADF-STEM images of the grain boundary in monolayer $NbSe_2$. **a** A tilted grain boundary with misorientation angle of 11°. Both atomically sharp lateral interconnected (*red rectangle*) and vertically stacked (*blue rectangle*) boundary regions are found to coexist. The *inset* shows the fast Fourier transformation (*FFT*) of the image. The distorted polygons are also highlighted in the *red rectangle*. *Scale bar*, 0.5 nm. **b** Selected FFT-filtered image of the two domains and their overlap images. The overlapped image confirms the coexistence of the two types of grain boundaries. *Scale bar*, 1 nm. **c** Similar tilted grain boundary without an overlapping region nearby. The *orange lines* indicate the five-seven dislocation pairs, which is consistent with the theoretical predictions of the grain boundary structure. *Scale bar*, 1 nm

monolayer $NbSe_2$ viewed from different angles. The as-deposited $NbSe_2$ crystals on SiO_2/Si are typically triangular or hexagonal in shape. Figure 1b shows the optical image of uniform hexagonal $NbSe_2$ crystals. A representative atomic force microscopy (AFM) measurement (*inset* of Fig. 1b) indicates the thickness of the $NbSe_2$ crystal is around 1.1 nm, which corresponds to a monolayer TMD[20, 28]. As shown in Fig. 1c, the lateral domain size of monolayer CVD-grown $NbSe_2$ can reach 0.2 mm, which is ~10^2 times as large as that of $NbSe_2$ prepared by MBE (<1 μm)[3, 27]. In addition to SiO_2/Si substrates, our CVD method can deposit $NbSe_2$ layers on arbitrary selenium-resistant crystalline and amorphous substrates, such as silicon (100), quartz, and CVD graphene (Supplementary Fig. 3). Different substrates may result in $NbSe_2$ flakes of varied morphologies (Supplementary Figs. 3 and 4), suggesting that the underlying substrate has an influence on the nucleation and growth of $NbSe_2$. Direct growth on diverse substrates makes it feasible to study the $NbSe_2$-substrate interaction and related properties.

The chemical states of the as-grown $NbSe_2$ samples were examined by X-ray photoemission spectroscopy (XPS) (Supplementary Fig. 5). Figure 1d is the Nb 3*d* core-level spectrum, and the two peaks at 203.4 and 206.1 eV can be assigned to Nb^{4+} $3d_{5/2}$ and Nb^{4+} $3d_{3/2}$ of $NbSe_2$[29]. The absence of Nb^{5+} $3d_{5/2}$ and Nb^{5+} $3d_{3/2}$ peaks at higher binding energy (from 207.3 to 211.0 eV) indicates that the sample was not oxidized[30]. The Se 3*d* core levels spectrum can be fitted with Se $3d_{5/2}$ (53.2 eV) and Se $3d_{3/2}$ (54.1 eV) peaks in agreement with the spectra of $NbSe_2$ (Fig. 1e)[29, 30]. Furthermore, the absence of Na 1*s* and Cl 2*p* peaks suggests that as-grown $NbSe_2$ was not contaminated by the NaCl precursor (Supplementary Fig. 6).

Tuning the thickness of $NbSe_2$ layers. In addition to producing monolayer $NbSe_2$, the proposed CVD method is also capable of acquiring $NbSe_2$ crystals with different thicknesses from 1.1 to 16 nm, which will be useful for investigating the thickness-dependent properties such as superconductivity, charge–density-wave order and their interplay in the 2D system. The $NbSe_2$ layer thickness was found to be sensitive to the heating temperature of selenium source (T_{Se}). A portable thermocouple thermometer was used to measure the selenium temperature during sample growth. Figure 1f-h shows the thickness distribution statistics and representative morphologies (*inset* of Fig. 1f-h and Supplementary Fig. 7) of $NbSe_2$ crystals grown with T_{Se} of (f) 300–340, (g) 360–420, and (h) 450–480 °C, respectively, while keeping all other growth parameters identical. Notably, the average thickness of obtained $NbSe_2$ increased with T_{Se}. Monolayer $NbSe_2$ crystals were obtained only when selenium was heated to 300–340 °C. In our experimental set-up, relatively higher T_{Se} will induce a higher flow rate of the selenium vapour. Therefore, these results indicate that the thickness of $NbSe_2$ films highly relies on the flow rate of the selenium vapour. Supplementary Fig. 8 shows AFM images of $NbSe_2$ crystals with different thicknesses up to 16.2 nm. Raman spectra of the as-grown crystals show two characteristic peaks of $NbSe_2$ (Supplementary Fig. 9), including the in-plane E_{2g} mode at about 250 cm^{-1} and the out-of-plane A_{1g} mode at about 225 cm^{-1}. The broad feature at about 180 cm^{-1} is described as a soft mode because of its frequency behavior with temperature[4, 31]. Thickness dependence of the Raman spectra of $NbSe_2$ is also shown in Supplementary Fig. 9. For monolayer $NbSe_2$, the Raman intensity of both A_{1g} and E_{2g} are very weak at room temperature. With the sample thickness increases, the intensity of A_{1g} and E_{2g} increase significantly.

Structural characterization. In order to examine the quality of the as-grown 2*H*-$NbSe_2$ atomic layers, the atomic structure and the chemical composition of the $NbSe_2$ layers were characterized by atomic resolution ADF-STEM imaging, electron energy-loss spectroscopy (EELS) and energy-dispersive X-ray spectrometry (EDX). Since a bare $NbSe_2$ monolayer film is sensitive to the ambient environment, we transferred the $NbSe_2$ flakes grown on SiO_2 substrate with graphene encapsulation (see "Methods" section), constructing a graphene/$NbSe_2$/graphene sandwich structure for STEM imaging. Such structures have been demonstrated to be effective in protecting sensitive monolayer materials from being oxidized[32]. Figure 2a shows a low magnification ADF-STEM image of a large area of monolayer $NbSe_2$ sandwiched by graphene (schematic shown in the *inset*), where little oxidization is observed. Figure 2b shows a zoom-in image of the same area with atomic resolution, displaying the hexagonal atomic lattice of alternating bright and dark spots, which corresponds, respectively, to the Se_2 and Nb atomic columns as indicated in the atomic model, confirming its hexagonal phase. Diselenium vacancy can be directly visualized by their distinguishable contrast within the image, as highlighted by the *red circles*. Since the STEM image contrast is directly related to the atomic number and the number of atoms of the imaged species, more types of intrinsic point defects can be identified by carefully examining the image contrast of each atomic column. Figure 2c shows the atomic resolution image of three major types of point defects found in the monolayer $NbSe_2$ film, which are diselenium vacancy (V_{Se_2}, *red*), monoselenium vacancy (V_{Se}, *blue*), and anti-site defect where a Se_2 column replaces the Nb (*yellow*). These intrinsic point defects are similar to those found in MoS_2 and $MoSe_2$ with the same hexagonal phase[33, 34] grown by CVD method. We can therefore calculate the defect concentration in certain area by counting the number of point defects. The defect concentration in Fig. 2b is estimated to be ~0.18 nm^{-2}, which is similar to the case in mechanical

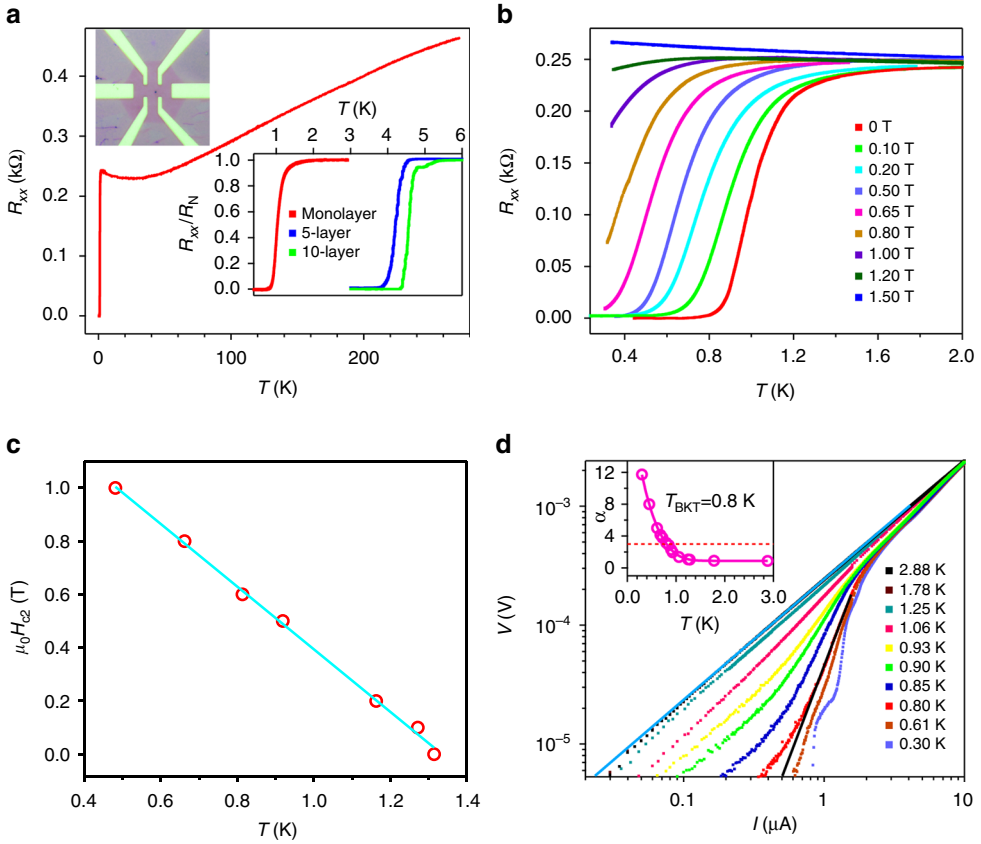

Fig. 4 Superconductivity in monolayer $NbSe_2$ devices. **a** Temperature dependence of the longitudinal resistance R_{xx} for sample A—a monolayer $NbSe_2$ device. *Upper left inset*: Optical image of a typical graphene protected monolayer $NbSe_2$ device. *Lower right inset*: Superconductivity in monolayer, 5-layer and 10-layer $NbSe_2$ devices. **b** Superconductivity of sample A in different magnetic fields. **c** Temperature dependence of the upper critical field H_{c2}. The *solid line* is the linear fit to H_{c2}. **d** Voltage–current (*V*-*I*) characteristic at different temperatures on a logarithmic scale. The *solid blue line* indicates the Ohmic behavior at high temperature. The *solid black line* represents the expected $V \propto I^3$ behavior at the Berezinskii-Kosterlitz-Thouless (BKT) transition. The *inset* shows the temperature-dependent exponent deduced from the power-law behavior, $V \propto I^{\alpha}$. As indicated by the *red dashed line*, α approaches 3 at $T = 0.8$ K

exfoliated monolayer materials[35], demonstrating the sufficiently low defect concentration in the film grown by our CVD method. The defect concentration is similar in multiple layer of $NbSe_2$, as shown in Supplementary Fig. 10.

We further study the stacking sequence in the CVD-grown $NbSe_2$ sample. Figure 2d shows two stacking orders that coexist in the bilayer region. While the lower bilayer is confirmed to be in $2H_a$ stacking, which is a stacking type commonly found in bulk $NbSe_2$, where Nb atoms are aligned to each other between the layers (atomic model in the *inset*), the upper bilayer is revealed to be in $2H_c$ stacking, similar to the $2H$ stacking in MoS_2. This is further evidenced by the equal intensity of each atomic column in the hexagonal rings, suggesting all the Nb atoms are aligned with the Se_2 columns between the layers. Nevertheless, we found the dominating stacking in bilayers is the $2H_a$ stacking phase. This result implies that, though $2H_c$ stacking is rarely seen in bulk, it can still form in the CVD process presumably due to the weak van der Waal interlayer interaction, which can be overcome by the rapid nucleation process. EDX and EELS were used to identify the chemical constituents of the as-grown layers. Figure 2e shows the region that is used to perform the EDX and EELS experiment. Both EDX and EELS unambiguously show the as-grown $NbSe_2$ film only contains Nb and Se without the presence of any other impurities (Fig. 2f, g). Similar defect and stacking structures are also observed in the $NbSe_2$ layers that are directly grown on graphene substrate, as shown in Supplementary Fig. 11.

Due to the protection of the graphene sandwich structure, we were able to directly observe the grain boundary structure in the air-sensitive $NbSe_2$ monolayer grown on SiO_2/Si by CVD method. Figure 3a displays a tilted grain boundary with a small misorientation angle (about 11°, determined by fast Fourier transform (FFT) in the *inset*). Interestingly, we found that two types of grain boundary structures coexist, as highlighted by different colored rectangles. The red region indicates the boundary that is atomically sharp, where two domains connects by distorted polygons to accommodate the strain due to the misorientation. The blue region represents another type of boundary, where the two domains overlap with each other, forming a vertically stacked structure. This is further evidenced by the selected FFT-filtered image shown in Fig. 3b, in which the two domains are separated according to the misorientation angles. Although both types of boundaries have been reported previously[36–38], it is commonly believed that only one of them can be formed depending on the dynamic energy between the growing frontiers of the misoriented domains during the growth process. The coexistence of both types in a single grain boundary structure suggests the formation energy between these two types of structures (atomically sharp and vertically stacked) is similar in $NbSe_2$, where their co-growth can be induced by local fluctuation of the growing conditions. Figure 3c shows a similar tilted grain boundary without overlapping regions nearby. The ideal five-seven dislocation pairs are found periodically embedded along the grain boundary (highlighted by *orange outline*), which is similar to the case of other TMD materials[34, 37] and consistent with the theoretical predictions[39]. In contrast, the polygons are found to be more distorted and did not have a periodic

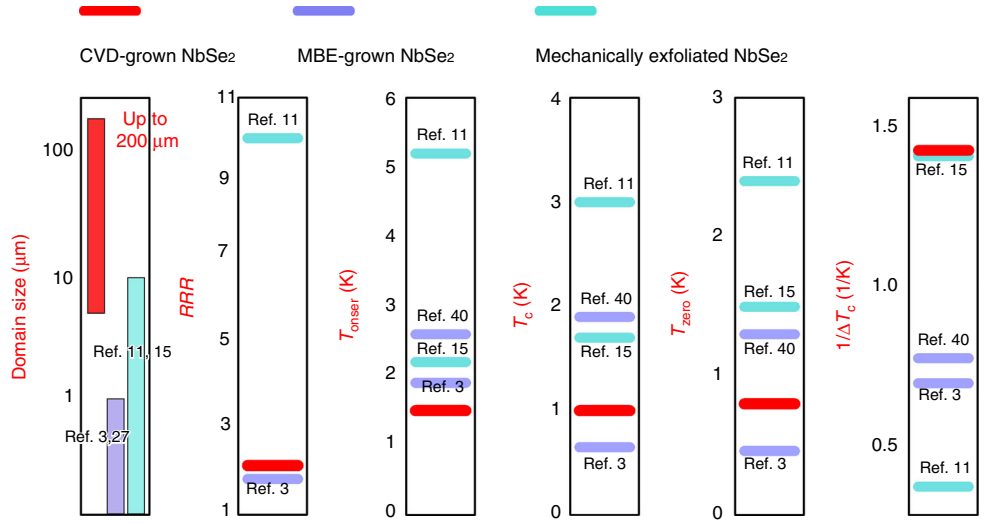

Fig. 5 Comparison of the superconducting performance of monolayer $NbSe_2$ prepared by CVD and other methods. From *left* to *right*: domain size, residual resistance ratio RRR, T_{onset}, T_c (0.5 R_N), T_{zero}, and $1/\Delta T_c$ for monolayer $NbSe_2$ samples prepared with different methods

distribution when the overlapping boundary is nearby, as shown in the red rectangular regions in Fig. 3a. This may be due to the alternation of the local strain profile in the atomically sharp grain boundary region induced by the overlapping area, which leads to the random formation of distorted polygons to release the inhomogeneous strain. These results reveal the local atomic structure of the grain boundaries, for the first time, in air-sensitive monolayer $NbSe_2$ which is hard to observe due to its easy oxidization without any protection.

Transport properties of mono- and few-layer $NbSe_2$. To further characterize the quality and dimensionality of as-grown $NbSe_2$ crystals, a low-temperature transport experiment was carried out on Hall-bar devices. Because of its air sensitivity[15], ultrathin $NbSe_2$ was first covered with a continuous monolayer graphene film before device fabrication (see "Methods" section). Figure 4a shows the temperature T dependence of longitudinal resistance R_{xx} for sample A—a representative monolayer $NbSe_2$ device (see Supplementary Note 1 and Supplementary Fig. 12 for more devices and data) at zero magnetic field. Consistent with previous studies[3, 11, 12], the sample shows a metallic behavior ($dR/dT > 0$) at high temperatures. At $T_{onset} = 1.5$ K, R_{xx} begins to decrease sharply and drops to zero at $T_{zero} = 0.8$ K, indicating the occurrence of superconductivity. Additionally, we find the superconducting transition in our high-quality $NbSe_2$ crystals can be tuned by changing the sample thickness. The *lower right inset* of Fig. 4a displays the normalized resistance R_{xx}/R_N as a function of temperature for $NbSe_2$ with different thickness. It is evident that the superconducting transition critical temperature T_c ($0.5R_N$) can be tuned from 4.56 K for 10-layer, 4.2 K for 5-layer, to 1.0 K for monolayer. Due to its sensitivity to moisture and oxygen, even when protected by graphene, the superconductivity of $NbSe_2$ sample degrades with increasing ambient exposure (Supplementary Fig. 13 and Supplementary Table 1), which is discussed in Supplementary Note 2.

To compare the quality of the monolayer $NbSe_2$ prepared with different methods, the residual resistance ratio (defined as the ratio of the room temperature resistance $R_{300\,K}$ to the normal-state resistance R_N) RRR, the superconducting transition onset temperature T_{onset}, the critical temperature T_c ($0.5R_N$), the zero-resistance temperature T_{zero}, and the inverse of the superconducting transition width $1/\Delta T_c$ are summarized in Fig. 5. It is noted that our CVD-grown monolayer $NbSe_2$ has a RRR = 2.0 very close to the reported value for MBE-grown $NbSe_2$[3], but the CVD sample has a T_{zero} (0.8 K) almost two times as high as that of MBE $NbSe_2$[3]. Though a much higher zero-resistance temperature $T_{zero} = 1.3$ K was reported in Se-capped MBE-grown monolayer $NbSe_2$, however, the resistance did not really drop to zero[40]. Besides, the ΔT_c in the CVD-grown sample is only 0.7 K, which is superior to all reported MBE $NbSe_2$[3, 40] and comparable to the best record in mechanically exfoliated samples[15]. The above data indicate that the CVD-grown $NbSe_2$ samples are high quality.

Figure 4b shows the temperature and field dependence of R_{xx} for sample A (see Supplementary Note 1 for more devices and data) with the field perpendicular to the sample plane. Under a magnetic field, the critical temperature T_c is defined by where the resistance is 90% of the normal state value R_N. With increasing the strength of magnetic field B, T_c shifts to lower temperatures. Finally, the superconductivity is completely suppressed with a magnetic field of about 1.5 T at $T = 0.3$ K. We summarize the H_{c2}-T_c phase diagram, where H_{c2} is the upper critical field, in Fig. 4c and find a linear relationship between H_{c2} and T_c, which is a characteristics of 2D superconductors[11–13] and can be explained by the standard linearized Ginzburg-Landau (GL) theory[41], $H_{c2}(T) = \frac{\phi_0}{2\pi\xi_{GL}(0)^2}\left(1 - \frac{T}{T_c}\right)$, where $\xi_{GL}(0)$ is the zero-temperature GL in-plane coherence length and ϕ_0 is the magnetic flux quantum. As shown in Fig. 4c, a linear fit between H_{c2} and T_c yields $\xi_{GL}(0) = 18$ nm (see Supplementary Note 3 and Supplementary Fig. 14 for more transport data of $NbSe_2$ grown on graphene substrate), which is about twice of the bulk value[16]. Based on the normal state resistance R_N and carrier density n_s as determined by Hall measurement (Supplementary Note 4 and Supplementary Fig. 15), the mean free path $l_m = 1.3$ nm can be obtained, smaller than that in exfoliated sample[12]. On the other hand, the normal state sheet resistance $R_s = 727\ \Omega$ (taken at $T_{onset} = 1.5$ K) is much smaller than the quantum resistance $R_q = h/4e^2 \approx 6.45\ k\Omega$, where e is the electron charge and h is Planck's constant, above which a disorder-induced superconductor-insulator transition emerges[42]. The above discussions indicate that our sample is in the low-disorder regime[11, 13, 40].

For a 2D superconductor with the thickness $d < \xi_{GL}(0)$, the superconducting phase transition is expected to be of the Berezinskii-Kosterlitz-Thouless (BKT) type[43, 44]. Figure 4d shows voltage–current (V-I) behavior as a function of temperature on a

log-log scale. The *V-I* relations change from a linear to a power-law dependence, $V \propto I^{\alpha}$ at T_c ($0.5R_N$), which is consistent with expectations for a 2D superconductor based on the theoretical model of the BKT transition. In the *inset* of Fig. 4d, we plot the exponent α vs. T, which is extracted from the slope of *V-I* traces. The BKT transition temperature T_{BKT} is estimated to be 0.8 K from where $\alpha = 3$ interpolates. The above data confirm that monolayer $NbSe_2$ exhibits the characteristics of a true 2D superconductor.

Discussion

The developed CVD growth technology has enabled the realization of superconductivity in non-UHV grown monolayer materials. Our results also provide a comprehensive understanding of the defect structure, superconducting performance as well as the influence of ambient-induced defects on superconductivity of $NbSe_2$. It is evident that even though low concentrations of selenium vacancy-related defects remained in the CVD-grown $NbSe_2$, they will not significantly affect the superconducting properties. Our facile CVD technology not only provides an excellent platform for the investigation of many fascinating properties of $NbSe_2$, but also holds promise for large-scale synthesis of 2D superconducting $NbSe_2$ films for potential device applications. Future developments may also include investigation and understanding of $NbSe_2$-substrate interplay and related novel properties, inspired by the research on 2D high-T_c Fe-chalcogenide superconductors[6, 7, 45] (more discussion in Supplementary Note 5). More recently, monolayer $NbSe_2$ was suggested as a candidate for realizing topological superconducting phase and engineering Majorana fermions[46, 47]. Therefore, the present work offers possibilities for the study of topological physics.

More importantly, our work indicates that a UHV environment is not necessarily required for the growth of monolayer superconductors. In our salt-assisted CVD synthesis of $NbSe_2$, the role of salt is particularly important as no nucleation of $NbSe_2$ can be observed without salt. It is noted that all niobium oxides have melting points above 1510 °C, which make them difficult to vaporize and react with selenium in the CVD process. The products of reactions between molten salts and metal (Mo[48], W[28], and Nb[49]) oxides have been investigated by several groups and found to be metal oxychlorides, which have much lower melting points compared with corresponding metal oxides[28, 48, 49]. Thus, it is suggested that in our CVD process, NaCl reacts with niobium oxides to give volatile niobium oxychloride[28], therefore increasing the vapour pressure of precursor and facilitating the growth of $NbSe_2$. With the proposed salt-assisted CVD method, a number of other 2D and even monolayer superconductors (2*H*-TaS_2, 2*H*-$TaSe_2$, 1*T*-$TiSe_2$, and 1*T*-Cu_xTiSe_2, etc.) could be synthesized by substituting niobium oxides with corresponding metal oxides precursors. Considering that most of the mentioned monolayers have never been synthesized (even by MBE) and investigated, the new growth technology will enrich the research field of 2D TMDs superconductivity greatly.

Methods

Atomically thin $NbSe_2$ crystals synthesis. We used partially oxidized niobium powder NbO_x ($x \leq 2.5$) as precursor for growing $NbSe_2$. In the first step, 5 g niobium powder (99.8%, 325 mesh, Alfa Aesar) was loaded into a both-ends-opened quartz tube equipped in a tube furnace. The niobium powder was ignited when furnace was heating to about 680 °C. After 1 min combustion, the niobium powder was rapid cooled to room temperature by moving it to cold zone. X-ray diffraction (XRD) analysis (Supplementary Fig. 2) indicated the obtained power consisted mainly of Nb, Nb_2O_5, and NbO.

Ambient pressure CVD growth of $NbSe_2$ was conducted in a 2-inch outer diameter fused quartz tube heated by a Lindberg/Blue M (HTF55322C) split-hinge furnace. Supplementary Fig. 1 shows the set-up of the CVD reaction chamber. The partially oxidized Nb powders NbO_x (0.7 g) together with NaCl powders (0.1 g) were placed in an alumina boat located in the center of the furnace. 285 nm SiO_2/Si or other substrates were placed 1-3 mm above the powder mixture with the polished side faced down. Selenium powder (2 g) (99.5%, Sigma-Aldrich) was placed at the upstream of the quartz tube, where the temperature ranges from 300 to 460 °C during the reaction. 120 sccm (cubic centimeters per minute) Ar and 24 sccm H_2 are used as carrier gases. The furnace is heated to 795 °C in 16 min and maintained at that temperature for 13 min to allow the synthesis of $NbSe_2$ layers. The furnace was naturally cooled to 680 °C without changing the carrier gases. Then the top cover of the furnace was opened to allow fast cooling of the sample, with carrier gases switched to 250 sccm Ar and 4 sccm H_2.

Device fabrication and transport measurements. For fabricating ultrathin $NbSe_2$ devices, large-area monolayer CVD graphene was used to cover and protect the thin $NbSe_2$ deposited on SiO_2/Si. First, a rectangular frame consisted by adhesive tape was attached to the poly (methyl methacrylate) (PMMA)-coated graphene grown on Cu foil[50]. Then PMMA/graphene was detached from the Cu substrate by a bubbling transfer method. The PMMA/graphene was rinsed in DI water for several times and then dried in air. Second, the PMMA/graphene film was directly attached to the $NbSe_2$ on SiO_2/Si substrate in an Ar-filled glove box, with the help of a drop of isopropanol added between. PMMA was then removed in acetone to form the graphene/$NbSe_2$ stacks. Finally, a fresh film of PMMA was deposited on the prepared graphene/$NbSe_2$ layers, by spin-coating at 3 K rpm for 1 min. The PMMA film was cured at 140 °C for 6 min in an Ar glove box. Hall bar device was made by electron-beam lithography and the contact metal (5 nm Cr/50 nm Au) was fabricated by electron-beam deposition.

The transport experiment is carried out in a top-loading helium-3 cryostat in a superconducting magnet. An AC probe current $I_{ac} = 10$ nA at 30.9 Hz is applied from the source to the drain. Then a lock-in amplifier monitors the longitudinal R_{xx} through two additional electrical contacts.

Fabrication of graphene/NbSe2/graphene sandwich cell for STEM imaging. First, mono- and few-layer $NbSe_2$ crystals were grown on 285 nm SiO_2/Si substrates. Second, with the same method described earlier in the device fabrication part, a continuous monolayer CVD graphene film was placed on top of the chip to form a graphene/$NbSe_2$-stacked heterostructure. Third, a thin PMMA film was spin-coated and cured on the chip, and then the PMMA/graphene/$NbSe_2$ film was detached from the SiO_2/Si substrate in HF. After rinsed in DI water, it was scooped up by a SiO_2/Si chip predeposited with monolayer graphene film to form a PMMA/graphene/$NbSe_2$/graphene structure on SiO_2/Si substrate. Fourth, the PMMA/graphene/$NbSe_2$/graphene film was detached from the substrate by etching SiO_2 layer in HF. After rinsed in DI water, it was scooped up by a TEM grid. Finally, the graphene/$NbSe_2$/graphene sandwich cell was created by removing PMMA in acetone.

Sample characterizations. XPS spectra were collected on a PHI Quantera II spectrometer using monochromatic Al-Kα ($h\upsilon = 1486.6$ eV) radiation, and the binding energies were calibrated with C 1s binding energy of 284.8 eV. AFM images were taken using the Asylum Research Cypher AFM in tapping mode. Raman spectra were recorded in vacuum by a Witec system with ×50 objective lens and a 2400 lines per mm grating under 532 nm laser excitation. The laser power was fixed at 1 mW. STEM experiments were performed by a low acceleration voltage JEOL 2100F equipped with Delta correctors and GIF quantum spectrometer.

Data availability. The data that support the findings of this study are available from the corresponding author on reasonable request.

Received: 18 October 2016 Accepted: 28 June 2017
Published online: 30 August 2017

References

1. Saito, Y., Nojima, T. & Iwasa, Y. Highly crystalline 2D superconductors. *Nat. Rev. Mater.* **2**, 16094 (2016).
2. Qin, S., Kim, J., Niu, Q. & Shih, C.-K. Superconductivity at the two-dimensional limit. *Science* **324**, 1314–1317 (2009).
3. Ugeda, M. M. et al. Characterization of collective ground states in single-layer NbSe2. *Nat. Phys.* **12**, 92–97 (2016).
4. Xi, X. et al. Strongly enhanced charge-density-wave order in monolayer $NbSe_2$. *Nat. Nano* **10**, 765–769 (2015).
5. Saito, Y., Kasahara, Y., Ye, J., Iwasa, Y. & Nojima, T. Metallic ground state in an ion-gated two-dimensional superconductor. *Science* **350**, 409–413 (2015).
6. Ge, J.-F. et al. Superconductivity above 100 K in single-layer FeSe films on doped $SrTiO_3$. *Nat. Mater.* **14**, 285–289 (2015).

7. Tan, S. et al. Interface-induced superconductivity and strain-dependent spin density waves in FeSe/$SrTiO_3$ thin films. *Nat. Mater.* **12**, 634–640 (2013).
8. Zhang, T. et al. Superconductivity in one-atomic-layer metal films grown on Si (111). *Nat. Phys.* **6**, 104–108 (2010).
9. Sekihara, T., Masutomi, R. & Okamoto, T. Two-dimensional superconducting state of monolayer Pb films grown on GaAs (110) in a strong parallel magnetic field. *Phys. Rev. Lett.* **111**, 057005 (2013).
10. Uchihashi, T., Mishra, P., Aono, M. & Nakayama, T. Macroscopic superconducting current through a silicon surface reconstruction with indium adatoms: Si (111)–(7×3)–. *Phys. Rev. Lett.* **107**, 207001 (2011).
11. Xi, X. et al. Ising pairing in superconducting NbSe2 atomic layers. *Nat. Phys.* **12**, 139–143 (2016).
12. Tsen, A. W. et al. Nature of the quantum metal in a two-dimensional crystalline superconductor. *Nat. Phys.* **12**, 208–212 (2016).
13. Xu, C. et al. Large-area high-quality 2D ultrathin Mo_2C superconducting crystals. *Nat. Mater.* **14**, 1135–1141 (2015).
14. Graybeal, J. M. Competition between superconductivity and localization in two-dimensional ultrathin a-MoGe films. *Phys. B+C* **135**, 113–119 (1985).
15. Cao, Y. et al. Quality heterostructures from two-dimensional crystals unstable in air by their assembly in inert atmosphere. *Nano Lett.* **15**, 4914–4921 (2015).
16. El-Bana, M. S. et al. Superconductivity in two-dimensional NbSe2 field effect transistors. *Supercond. Sci. Technol.* **26**, 125020 (2013).
17. Lee, Y.-H. et al. Synthesis and transfer of single-layer transition metal disulfides on diverse surfaces. *Nano Lett.* **13**, 1852–1857 (2013).
18. Zhang, Y. et al. Controlled growth of high-quality monolayer WS_2 layers on sapphire and imaging its grain boundary. *ACS Nano* **7**, 8963–8971 (2013).
19. Huang, J.-K. et al. Large-area synthesis of highly crystalline WSe2 monolayers and device applications. *ACS Nano* **8**, 923–930 (2013).
20. Zhang, M. et al. Controlled synthesis of ZrS_2 monolayer and few layers on hexagonal boron nitride. *J. Am. Chem. Soc.* **137**, 7051–7054 (2015).
21. Li, X. et al. Controlled vapor phase growth of single crystalline, two-dimensional GaSe crystals with high photoresponse. *Sci. Rep.* **4**, 5497 (2014).
22. Zhou, X. et al. Ultrathin $SnSe_2$ flakes grown by chemical vapor deposition for high-performance photodetectors. *Adv. Mater.* **27**, 8035–8041 (2015).
23. Duan, X. et al. Lateral epitaxial growth of two-dimensional layered semiconductor heterojunctions. *Nat. Nano* **9**, 1024–1030 (2014).
24. Yu, Y. et al. Controlled scalable synthesis of uniform, high-quality monolayer and few-layer MoS2 films. *Sci. Rep.* **3**, 1866 (2013).
25. Kim, A. R. et al. Alloyed 2D metal-semiconductor atomic layer junctions. *Nano Lett.* **16**, 1890–1895 (2016).
26. Kim, Y. et al. Alloyed 2D metal–semiconductor heterojunctions: origin of interface states reduction and schottky barrier lowering. *Nano Lett.* **16**, 5928–5933 (2016).
27. Hotta, T. et al. Molecular beam epitaxy growth of monolayer niobium diselenide flakes. *Appl. Phys. Lett.* **109**, 133101 (2016).
28. Li, S. et al. Halide-assisted atmospheric pressure growth of large WSe_2 and WS_2 monolayer crystals. *Appl. Mater. Today* **1**, 60–66 (2015).
29. Wertheim, G., DiSalvo, F. & Buchanan, D. Site inequivalence in Fe 1+x Nb 3– x Se 10. *Phys. Rev. B* **28**, 3335 (1983).
30. Boscher, N. D., Carmalt, C. J. & Parkin, I. P. Atmospheric pressure chemical vapour deposition of $NbSe_2$ thin films on glass. *Eur. J. Inorg. Chem.* **2006**, 1255–1259 (2006).
31. Tsang, J., Smith, J. Jr & Shafer, M. Raman spectroscopy of soft modes at the charge-density-wave phase transition in 2 H–Nb Se 2. *Phys. Rev. Lett.* **37**, 1407 (1976).
32. Nguyen, L. et al. Atomic defects and doping of monolayer $NbSe_2$. *ACS Nano* **11**, 2894–2904 (2017).
33. Zhou, W. et al. Intrinsic structural defects in monolayer molybdenum disulfide. *Nano Lett.* **13**, 2615–2622 (2013).
34. Lu, X. et al. Large-area synthesis of monolayer and few-layer $MoSe_2$ films on SiO_2 substrates. *Nano Lett.* **14**, 2419–2425 (2014).
35. Hong, J. et al. Exploring atomic defects in molybdenum disulphide monolayers. *Nat. Commun.* **6**, 6293 (2015).
36. Li, X. et al. Two-dimensional GaSe/$MoSe_2$ misfit bilayer heterojunctions by van der Waals epitaxy. *Sci. Adv.* **2**, e1501882 (2016).
37. Najmaei, S. et al. Vapour phase growth and grain boundary structure of molybdenum disulphide atomic layers. *Nat. Mater.* **12**, 754–759 (2013).
38. van der Zande, A. M. et al. Grains and grain boundaries in highly crystalline monolayer molybdenum disulphide. *Nat. Mater.* **12**, 554–561 (2013).
39. Zou, X., Liu, Y. & Yakobson, B. I. Predicting dislocations and grain boundaries in two-dimensional metal-disulfides from the first principles. *Nano Lett.* **13**, 253–258 (2012).
40. Onishi, S. et al. Selenium capped monolayer $NbSe_2$ for two-dimensional superconductivity studies. *Phys. Status Solidi B* **253**, 2396–2399 (2016).
41. Tinkham, M. *Introduction to Superconductivity* (Courier Corporation, 1996).
42. Fiory, A. & Hebard, A. Electron mobility, conductivity, and superconductivity near the metal-insulator transition. *Phys. Rev. Lett.* **52**, 2057–2060 (1984).
43. Reyren, N. et al. Superconducting interfaces between insulating oxides. *Science* **317**, 1196–1199 (2007).
44. Halperin, B. & Nelson, D. R. Resistive transition in superconducting films. *J. Low Temp. Phys.* **36**, 599–616 (1979).
45. Miyata, Y., Nakayama, K., Sugawara, K., Sato, T. & Takahashi, T. High-temperature superconductivity in potassium-coated multilayer FeSe thin films. *Nat Mater.* **14**, 775–779 (2015).
46. He, W.-Y., Zhou, B. T., He, J. J., Zhang, T. & Law, K. Nodal topological superconductivity in monolayer $NbSe_2$. Preprint at http://arxiv.org/abs/1604.02867 (2016).
47. Zhou, B. T., Yuan, N. F., Jiang, H.-L. & Law, K. T. Ising superconductivity and Majorana fermions in transition-metal dichalcogenides. *Phys. Rev. B* **93**, 180501 (2016).
48. Manukyan, K. V. et al. Mechanism of molten-salt-controlled thermite reactions. *Ind. Eng. Chem. Res.* **50**, 10982–10988 (2011).
49. Gaune-Escard, M. & Haarberg, G. M. *Molten Salts Chemistry and Technology* (John Wiley & Sons, 2014).
50. Li, X. S. et al. Large-area synthesis of high-quality and uniform graphene films on copper foils. *Science* **324**, 1312–1314 (2009).

Acknowledgements

This work is supported by the Singapore National Research Foundation under NRF RF Award No. NRF-RF2013-08, the start-up funding from Nanyang Technological University (M4081137.070), Tier 2 MOE2016-T2-2-153, MOE2016-T2-1-131 (S), MOE2015-T2-2-007, Tier 1 RG164/15, and CoE Industry Collaboration Grant WINTECH-NTU. The work at IOP was supported by the National Basic Research Program of China from the MOST under the Grant nos. 2014CB920904, 2015CB921101, and 2013CB921702, by the NSFC under the Grant nos. 11174340 and 91421303. J.L. and K.S. acknowledge JST-ACCEL and JSPS KAKENHI (JP16H06333 and P16823) for financial support. Y.C. and T.Y. thank the support of Ministry of Education AcRF Tier 1 RG100/15.

Author contributions

Z.L., G.L., and E.H.T.T. directed the research; H.W. and Z.L. proposed and designed the experiments; H.W. performed the $NbSe_2$ and $NbSe_2$/graphene heterostructure synthesis and did the SEM, AFM, and XPS measurements; X.H., J.C., and G.L. did the superconductivity measurements and data analysis; X.H., C.Z., Q.Z., and F.L. contributed to the device fabrication; J.L. did the STEM measurement and data analysis; Y.C. and H.W. did the Raman measurement; H.W. and J.Z. prepared the STEM sample; P.Y. and X.W. did the XRD measurement; H.H., S.H.T., W.G., K.S., F.M., C.Y., L.L., T.Y., and E.H.T.T. contributed to the results analysis and discussions. H.W., J.L., G.L., and Z.L. co-wrote the paper with input from all authors.

Additional information

Supplementary Information accompanies this paper at doi:10.1038/s41467-017-00427-5.

Competing interests: The authors declare no competing financial interests.

Reprints and permission information is available online at http://npg.nature.com/reprintsandpermissions/

Publisher's note: Springer Nature remains neutral with regard to jurisdictional claims in published maps and institutional affiliations.